Original Article

# Multiparametric dual-energy CT to differentiate stage T1 nasopharyngeal carcinoma from benign hyperplasia

**Hesong Shen[1], Xiaoqian Yuan[1], Daihong Liu[1], Chunrong Tu[1], Xing Wang[1], Renwei Liu[1], Xiaoxia Wang[1], Xiaosong Lan[1], Kaiwen Fu[2], Jiuquan Zhang[1]**

[1]Department of Radiology, Chongqing University Cancer Hospital & Chongqing Cancer Institute & Chongqing Cancer Hospital, Chongqing, China; [2]Department of Pathology, Chongqing University Cancer Hospital & Chongqing Cancer Institute & Chongqing Cancer Hospital, Chongqing, China

*Contributions:* (I) Conception and design: H Shen; (II) Administrative support: J Zhang; (III) Provision of study materials or patients: C Tu, X Wang, R Liu; (IV) Collection and assembly of data: X Wang, K Fu; (V) Data analysis and interpretation: D Liu, X Lan; (VI) Manuscript writing: All authors; (VII) Final approval of manuscript: All authors.

*Correspondence to:* Jiuquan Zhang. Department of Radiology, Chongqing University Cancer Hospital & Chongqing Cancer Institute & Chongqing Cancer Hospital, Chongqing 400030, China. Email: zhangjq_radiol@foxmail.com.

**Background:** Stage T1 nasopharyngeal carcinoma ($NPC_{T1}$) and benign hyperplasia (BH) are 2 common causes of nasopharyngeal mucosa/submucosa thickening without specific clinical symptoms. The treatment management of these 2 entities is significantly different. Reliable differentiation between the 2 entities is critical for the treatment decision and prognosis of patients. Therefore, our study aims to explore the optimal energy level of noise-optimized virtual monoenergetic images [VMI (+)] derived from dual-energy computed tomography (DECT) to display $NPC_{T1}$ and BH and to explore the clinical value of DECT for differentiating these 2 diseases.

**Methods:** A total of 91 patients (44 $NPC_{T1}$, 47 BH) were enrolled. The demarcation of the lesion margins and overall image quality, noise, contrast-to-noise ratio (CNR), and signal-to-noise ratio (SNR) were evaluated for 40–80 kiloelectron volts (keV) VMIs (+) and polyenergetic images in the contrast-enhanced phase. Image features were assessed in the contrast-enhanced images with optimal visualization of $NPC_{T1}$ and BH. The demarcation of $NPC_{T1}$ and BH in iodine-water maps was also assessed. The contrast-enhanced images were used to calculate the slope of the spectral Hounsfield unit curve ($\lambda_{HU}$) and normalized iodine concentration (NIC). The nonenhanced phase images were used to calculate the normalized effective atomic number ($NZ_{eff}$). The attenuation values on 40–80 keV VMIs (+) in the contrast-enhanced phase were recorded. The diagnostic performance was assessed using receiver operating characteristic (ROC) curve analysis.

**Results:** The 40 keV VMI (+) in the enhanced phase yielded higher demarcation of the lesion margins scores, overall image quality scores, noise, SNR, and CNR values than 50–80 keV VMIs (+) and polyenergetic images. $NPC_{T1}$ yielded higher attenuation values on VMI (+) at 40 keV ($A_{40}$), NIC, $\lambda_{HU}$, and $NZ_{eff}$ values than BH. The multivariate logistic regression model combining image features (tumor symmetry) with quantitative parameters ($A_{40}$, NIC, $\lambda_{HU}$, and $NZ_{eff}$) yielded the best performance for differentiating the 2 diseases (AUC: 0.963, sensitivity: 89.4%, specificity: 93.2%).

**Conclusions:** The combination of DECT-derived image features and quantitative parameters contributed to the differentiation between $NPC_{T1}$ and BH.

**Keywords:** Virtual monoenergetic images (VMI); dual-energy computed tomography (DECT); nasopharyngeal carcinoma (NPC); benign hyperplasia (BH)

Submitted Nov 16, 2020. Accepted for publication Apr 19, 2021.
doi: 10.21037/qims-20-1269
**View this article at:** http://dx.doi.org/10.21037/qims-20-1269

## Introduction

Stage T1 nasopharyngeal carcinoma ($NPC_{T1}$) and benign hyperplasia (BH) are 2 common causes of nasopharyngeal mucosa/submucosa thickening without specific clinical symptoms (1). The treatment management of these 2 entities is significantly different. $NPC_{T1}$ is treated with radical radiotherapy, and BH requires no specific treatment (2). Therefore, reliable differentiation between the 2 entities is critical for the treatment decision and prognosis of patients.

The definitive differential diagnosis of NPC and BH is reached through endoscopic-guided biopsy (3). However, an endoscopic biopsy is limited due to its invasiveness and bleeding risk (4).

Magnetic resonance imaging (MRI) is a noninvasive tool used for differentiating $NPC_{T1}$ and BH (5). However, the diagnostic accuracy of MRI is limited for these 2 entities due to the considerable overlap of MRI features such as diffuse symmetrical wall thickening of the nasopharynx (1,6-8). Moreover, the wider application of MRI is limited by its high cost.

As a recent and noninvasive imaging modality, dual-energy computed tomography (DECT) can provide additional image reconstructions such as virtual monoenergetic images (VMI) with different kiloelectron volts (keV) (9,10). Increasing evidence indicates that VMI at 40 keV can improve the visualization of tumors and their boundaries in head and neck cancers (11-13). Moreover, a novel noise-optimized VMI reconstruction algorithm [VMIs (+)] can further improve image quality at low-keV levels (14,15). On the other hand, DECT can provide a variety of quantitative parameters of tumor characteristics, including the normalized iodine concentration (NIC), the slope of the spectral Hounsfield unit curve ($\lambda_{HU}$), and the normalized effective atomic number ($NZ_{eff}$) (16-19), allowing for accurate differential diagnoses in head and neck neoplasms (20-22).

The optimal keV of VMI (+) to display the delineations of $NPC_{T1}$ and BH is unknown but would be very useful for accurately delineating the target area of radiotherapy and for improving the prognosis of patients. Therefore, our study aims to explore the optimal keV of VMI (+) derived from DECT for the visualization of $NPC_{T1}$ and BH and to investigate the clinical value of imaging features and quantitative parameters in differentiating the 2 entities.

## Methods

### *Patients*

The study was conducted in accordance with the Declaration of Helsinki (as revised in 2013). This study was approved by our hospital's review committee, and written informed consent was obtained.

A total of 44 patients (33 males, 11 females; mean age, 49 years; range, 28–68 years) with $NPC_{T1}$ and 47 patients (33 males, 14 females; mean age, 42 years; range, 23–60 years) with BH were enrolled between October 2018 and April 2020. All patients underwent a DECT examination. Eligibility criteria were as follows: (I) histopathologically confirmed $NPC_{T1}$s and BHs; (II) $NPC_{T1}$ with the tumor confined to the nasopharynx or only extending to the oropharynx and/or nasal fossa according to the 8th edition of the American Joint Committee on Cancer TNM Staging System (23); and (III) no treatments before registration. The exclusion criteria were as follows: (I) DECT images were not available because of severe artifacts; (II) the mucosal thickness was less than 3 mm.

### *DECT image acquisition*

Dual-phase (nonenhanced phase and contrast-enhanced phase) DECT scans from the bottom of the frontal sinus to the oral pharynx were acquired with a dual-source CT scanner (SOMATOM Drive, Siemens Healthineers, Germany). The tube voltages were set at 100 kVp and Sn140 kVp (adding the tin filter). Advanced model-based iterative reconstruction (strength, 3) and automatic current modulation (CARE Dose 4D, Siemens Healthineers Germany) were used. The detailed parameters were described in our previous study in nasopharyngeal dual-energy CT (24).

Iodine contrast media (Loversol, 320 mg/mL, HENGRUI Medicine, Jiangsu, China) was administered through the right or left ulnar vein by a dual-head injector. The dosage was 1.5 mL/kg, and the flow rate was 2.5 mL/s, followed by 20 mL of 0.9% normal saline administered at the same flow rate. Contrast-enhanced phase imaging began 30 s after a threshold of 100 HU in the aortic arch using a bolus-tracking technique.

### *DECT image reconstruction*

The postprocessing of CT images was performed on a

 

syngo.via workstation (syngo.via VB20A, Dual Energy, Siemens Healthineers, Germany). A mix factor of 0.4 (M_0.4; 40% of the low kV and 60% of the high-kV spectrum) was used for standard polyenergetic image (PEI) reconstruction. VMIs (+) were reconstructed at 40–80 keV levels with an interval of 10 in the contrast-enhanced phase because 40–70 keV VMIs (+) were recommended for visualization of soft tissue lesions in previous studies (11,12,22). The effective atomic number maps were reconstructed using the nonenhanced phase images, and the iodine-water maps with an iodine concentration (IC) of 100% were reconstructed using the phase of the contrast-enhanced image. Transverse sections were reconstructed for all series using the following parameters: thickness, 1.5 mm; increment, 1.2 mm; and soft-tissue kernel, J30f. These series were then transmitted to the local picture archiving and communication systems. Two radiologists, readers 1 and 2 with 10 and 15 years of experience, respectively, qualitatively and quantitatively reviewed the DECT data.

### *Subjective image quality assessment*

Two radiologists independently analyzed 40–80 keV VMIs (+), PEI (M_0.4), and iodine-water maps with an IC of 100%. Reader 1 analyzed images twice at an interval of 1 month. The assessment of subjective image quality included the overall image quality and demarcation of the lesion margins. Using a 5-point Likert scale, the overall image quality (1, unacceptable; 2, suboptimal; 3, adequate; 4, good; and 5, excellent) and demarcation of the lesion margin (ranging from 1 = no visual demarcation to 5 = perfect demarcation of contours) were respectively scored.

### *Objective image quality assessment*

Quantitative analyses were performed on the VMIs (+) at 40–80 keV and PEI (M_0.4). Noise, signal-to-noise ratio (SNR) and contrast-to-noise ratio (CNR) were analyzed by 2 radiologists who were blinded to the histopathological and clinical data. Reader 1 analyzed images twice at an interval of 1 month. Both readers placed regions of interest (ROIs), avoiding any area of gross necrosis, within the following regions: nasopharyngeal lesion and right lateral pterygoid muscle on the images of the contrast-enhanced phase. The standard deviation (SD) of attenuation values in the right lateral pterygoid muscle was defined as the noise of images. The formulas used to assess image quality quantitatively are as follows:

- Noise = $SD_{\text{right lateral pterygoid muscle}}$;
- SNR = $HU_{\text{nasopharyngeal lesions}}/SD_{\text{right lateral pterygoid muscle}}$;
- CNR = $(HU_{\text{nasopharyngeal lesions}} - HU_{\text{right lateral pterygoid muscle}})/SD_{\text{right lateral pterygoid muscle}}$.

### *Image features of DECT assessment*

The image features of DECT, including tumor symmetry, density homogeneity, and degree of enhancement, were independently assessed by 2 radiologists. Reconstruction with the highest subjective image quality scores, SNR and CNR, in 40–80 keV VMIs (+) and PEI was used for image feature assessment of NPC and BH. Tumor symmetry, density homogeneity, and degree of enhancement were classified according to our previous DECT study in the nasopharynx (24).

### *Quantitative parameters of DECT assessment*

Two radiologists independently analyzed iodine-water maps, effective atomic number maps, VMIs (+) at 40–80 keV, and PEI (M_0.4) data. Reader 1 analyzed images twice at an interval of 1 month. ROIs (mean area, 145.67±28.24 $mm^2$; range, 57–358 $mm^2$) were placed at the largest diameter slice of the primary lesion on the axial images and included as much of the lesion as possible and avoided the necrosis areas. The IC values of nasopharyngeal lesions and the internal jugular vein were measured in the "VNC" mode at the syngo.via workstation by using the original contrast-enhanced images. NIC = IC value of the nasopharyngeal lesions/IC value of the internal jugular vein. The $Z_{eff}$ values were measured in the "Rho/$Z_{eff}$" mode at the syngo.via workstation by using the nonenhanced phase images. $NZ_{eff}$ = $Z_{eff}$ value of the nasopharyngeal lesions/$Z_{eff}$ value of the internal jugular vein.

The attenuation values of nasopharyngeal lesions on VMIs (+) at 40–80 keV ($A_{40}$, $A_{50}$, $A_{60}$, $A_{70}$, and $A_{80}$) were measured. The $\lambda_{HU}$ values of primary lesions were calculated with the following formula: $\lambda_{HU} = (A_{40} - A_{80})/40$. The attenuation values of nasopharyngeal lesions in unenhanced ($A_n$) and enhanced ($A_e$) PEIs were also measured. $A_e$ minus $A_n$ was $\Delta A$.

### *Statistical analysis*

SPSS statistics version 25.0 software (IBM, Armonk, US) was used for statistical analyses. The quadratic weighted Cohen's kappa coefficient (κ) was used for intra- and inter-

 

reader agreement of the overall image quality, demarcation of the lesion margins, and image feature assessment (κ=0.81–1.00, excellent; κ=0.61–0.80, substantial; κ=0.41–0.60, moderate, κ=0.21–0.40, fair, κ=0.00–0.20, poor). The intra- and inter-reader reproducibility of the noise, SNR, CNR, attenuation, NIC, $NZ_{eff}$, and $\lambda_{HU}$ values were evaluated by the intraclass correlation coefficient (ICC). Qualitative data were compared by the $\chi^2$ test. The Kolmogorov-Smirnov test was used for the assessment of the normality of quantitative data distribution. The differences between quantitative data were compared using the independent sample *t*-test and one-way ANOVA with the Bonferroni post hoc test for normal distribution data and the Mann-Whitney U test and nonparametric Kruskal-Wallis test with Bonferroni post hoc test for nonnormal distribution data. Receiver operating characteristic (ROC) curve analysis was performed to assess the DECT parameters' performance in distinguishing $NPC_{T1}$ and BH. The Youden index determined the optimal threshold, and the area under the curve (AUC), sensitivity, and specificity were calculated. The Delong test was used to assess the differences in AUCs. The independent predictive parameters for discriminating the 2 entities were determined by binary logistic regression analysis. A two-sided P value <0.05//N (N represented the number of groups to compare) was considered statistically significant in the Bonferroni post hoc test, and a two-sided P value <0.05 was considered statistically different in the other tests.

## Results

### *Patient characteristics*

Of the 111 patients, 20 patients were excluded because of a history of antitumor therapy before DECT examination (n=15), unsatisfactory image quality (n=4), and mucosal thickness inferior to 3 mm (n=1). The final enrolled patients consisted of 44 $NPC_{T1}$ patients and 47 BH patients. There were no intergroup differences in terms of age and sex, and the P values were 0.061 and 0.422, respectively.

The average cumulative CT dose index ($CTDI_{vol}$) and dose length product (DLP) for the enrolled patients were 11.7±2.5 mGy and 106.5±24.6 mGy cm, respectively.

### *Subjective image quality assessment*

The lesion margin's overall image quality and demarcation showed excellent intra- and inter-reader agreement (κ values ranged from 0.806 to 0.935).

The 40 keV VMI (+) in the enhanced phase yielded higher demarcation of the lesion margins scores and overall image quality scores than 50–80 keV VMIs (+) and PEI (M_0.4) (all P values <0.001; *Table 1* and *Figures 1*,*2*). The 40 keV VMI (+) yielded higher demarcation of lesion margin scores than iodine-water maps with an IC of 100% (P value <0.001; *Table 1*).

### *Objective image quality assessment*

Intra- and inter-reader agreements were excellent for noise, SNR, and CNR (ICC values ranged from 0.836 to 0.935).

The 40 keV VMI (+) yielded higher noise, SNR, and CNR than 50–80 keV VMIs (+) and PEI (M_0.4), as shown in *Table 2* and *Figure 3* (all P values <0.001).

### *Image features of DECT assessment*

Intra- and inter-reader agreements were excellent for assessing image features (κ values ranged from 0.813 to 0.902).

Tumor symmetry showed a significant difference between $NPC_{T1}$ and BH (P<0.001). Density homogeneity and degree of enhancement (high, intermediate, and low) showed no differences between $NPC_{T1}$ and BH (P values were 0.245, 0.947, 0.321, and 0.325, respectively), as shown in *Table 3*.

### *Quantitative parameters of DECT assessment*

Intra- and inter-reader agreements were excellent for the NIC, $\lambda_{HU}$, $NZ_{eff}$, $A_{40}$, $A_{50}$, $A_{60}$, $A_{70}$, $A_{80}$, $A_n$, $A_e$, and ΔA (ICC values ranged from 0.809 to 0.913).

Compared with BH, $NPC_{T1}$ yielded higher $A_{40}$, NIC, $\lambda_{HU}$, and $NZ_{eff}$ values (all P values <0.001). There were no significant differences in terms of $A_{50}$, $A_{60}$, $A_{70}$, $A_{80}$, $A_n$, $A_e$, and ΔA values between $NPC_{T1}$ and BH, with P values of 0.057, 0.113, 0.068, 0.281, 0.117, 0.513, and 0.115, respectively, as shown in *Table 4* and *Figures 4*,*5*.

### *Diagnostic performances of combined image features with quantitative parameters*

Tumor symmetry successfully differentiated $NPC_{T1}$ from BH (AUC: 0.691, sensitivity: 63.6%; specificity: 68.7%). The NIC yielded a higher AUC, sensitivity, and specificity than $\lambda_{HU}$, $NZ_{eff}$, and $A_{40}$ (AUC: 0.825 *vs.* 0.744 *vs.* 0.732

 

**Table 1** Objective image characteristics for noise-optimized monoenergetic images (40–80 keV), polyenergetic images with a mix factor of 0.4 (M_0.4), and iodine-water maps with an iodine concentration of 100%

| Score | 40 keV | 50 keV | 60 keV | 70 keV | 80 keV | M_0.4 | Iodine-water maps | P value |
|---|---|---|---|---|---|---|---|---|
| Overall image quality | | | | | | | | |
| 1 | 0 | 0 | 0 | 0 | 0 | 0 | | |
| 2 | 0 | 0 | 2 | 5 | 14 | 11 | | |
| 3 | 0 | 15 | 17 | 35 | 54 | 56 | | |
| 4 | 19 | 25 | 69 | 51 | 23 | 24 | | |
| 5 | 72 | 51 | 3 | 0 | 0 | 0 | | |
| Total | 436 | 400 | 346 | 319 | 282 | 286 | | |
| Mean ± SD | 4.8±0.4 | 4.4±0.7 | 3.8±0.6 | 3.5±0.6 | 3.1±0.5 | 3.1±0.6 | | <0.001 |
| Demarcation of lesion margins | | | | | | | | |
| 1 | 0 | 0 | 0 | 0 | 1 | 1 | 0 | |
| 2 | 0 | 0 | 1 | 5 | 26 | 30 | 3 | |
| 3 | 2 | 17 | 37 | 68 | 63 | 59 | 39 | |
| 4 | 23 | 39 | 32 | 13 | 1 | 1 | 43 | |
| 5 | 66 | 35 | 21 | 5 | 0 | 0 | 6 | |
| Total | 428 | 382 | 346 | 291 | 246 | 242 | 325 | |
| Mean ± SD | 4.7±0.5 | 4.2±0.7 | 3.8±0.8 | 3.2±0.7 | 2.7±0.5 | 2.7±0.5 | 3.8±0.8 | <0.001 |

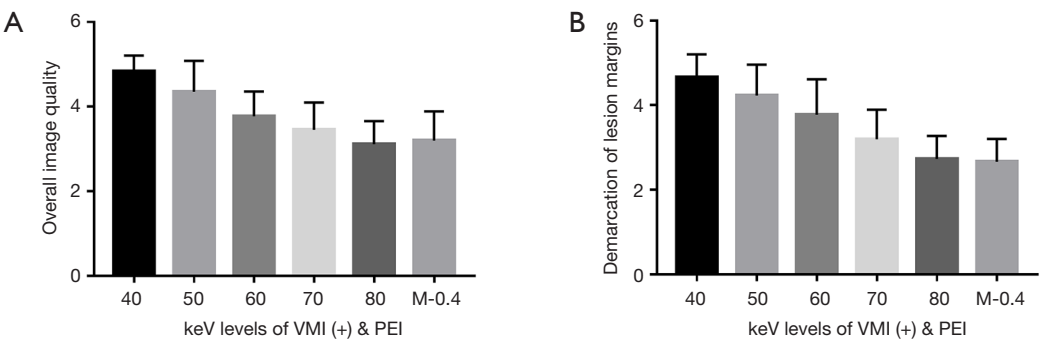


**Figure 1** Subjective image characteristics for VMIs (+) at 40–80 keV and PEI (M_0.4). The 40 keV VMI (+) reconstructed by contrast-enhanced phase images yielded the highest overall image quality scores (A) and demarcation of lesion margins scores (B) compared with 50–80 keV VMIs (+) and PEI (M_0.4). VMI (+), noise-optimized virtual monoenergetic images; keV, kiloelectron volt; PEI (M_0.4), polyenergetic images with a mix factor of 0.4.

*vs.* 0.727, sensitivity: 79.51% *vs.* 70.5% *vs.* 68.2% *vs.* 72.7%, specificity: 74.5% *vs.* 68.1% *vs.* 68.1% *vs.* 61.7%, all P values <0.001). The multivariate logistic regression model combining image features (tumor symmetry) with quantitative parameters ($A_{40}$, NIC, $\lambda_{HU}$, and $NZ_{eff}$) yielded higher AUC (0.963), sensitivity (89.4%), and specificity (93.2%) values than any 1 parameter alone for differentiating $NPC_{T1}$ from BH, as shown in *Table 5* and *Figure 6*. In terms of AUC, all P values were less than 0.05, as shown in *Table 5* and *Figure 6*. The cutoff values of the above parameters for differentiating $NPC_{T1}$ from BH are also shown in *Table 5*.

 

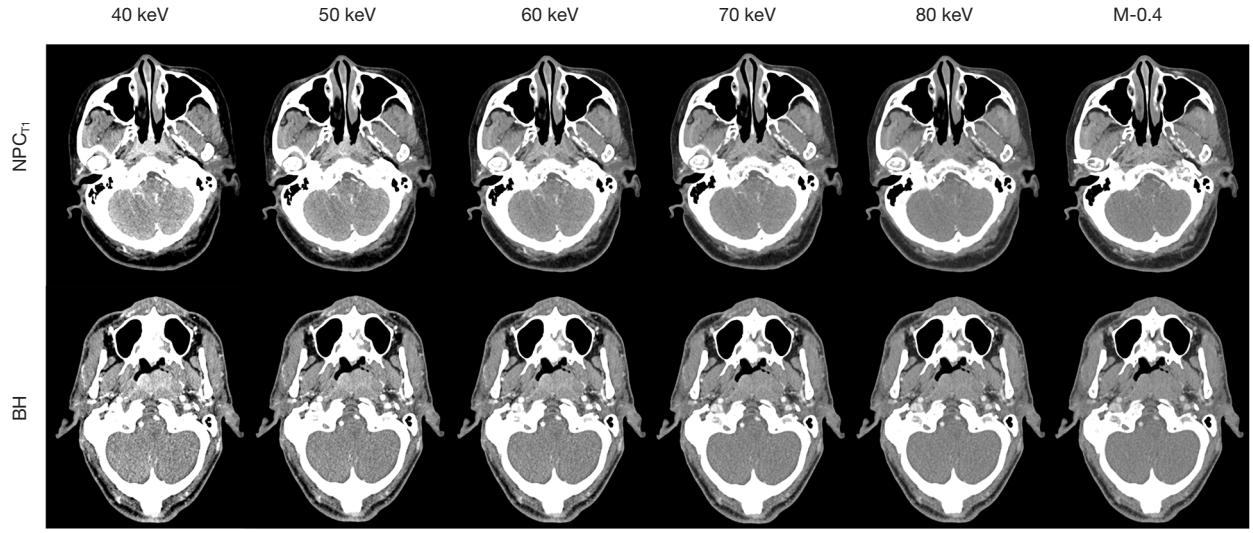


**Figure 2** Axial enhanced phase images of the 40–80 keV VMIs (+) and PEI (M_0.4) for a 65-year-old man with NPCT1 and a 50-year-old woman with BH. The 40 keV VMI (+) yielded the highest subjective image quality scores compared with 50–80 keV VMIs (+) and PEI (M_0.4). VMI (+), noise-optimized virtual monoenergetic images; keV, kiloelectron volt; PEI (M_0.4), polyenergetic images with a mix factor of 0.4; NPCT1, stage T1 nasopharyngeal carcinoma; BH, benign hyperplasia.

**Table 2** Objective image characteristics for noise-optimized monoenergetic images (40–80 keV) and polyenergetic images with a mix factor of 0.4 (M_0.4)

| Variable | 40 keV | 50 keV | 60 keV | 70 keV | 80 keV | M_0.4 | P value[†] |
|---|---|---|---|---|---|---|---|
| Noise (HU) | 20.70 (17.80–23.95) | 18.27 (14.73–20.83) | 16.13 (14.30–17.82) | 15.06 (12.16–17.30) | 13.56 (10.34–15.55) | 12.32 (11.19–13.56) | <0.001 |
| SNR | 15.52 (14.96–16.35) | 13.44 (13.09–14.13) | 10.99 (10.07–11.76) | 8.03 (7.63–8.79) | 6.65 (5.71–7.28) | 6.80 (5.87–7.53) | <0.001 |
| CNR | 7.39 (7.00–7.81) | 5.91 (5.57–5.50) | 4.90 (4.55–5.28) | 3.44 (3.19–3.76) | 1.95 (1.69–2.52) | 2.13 (1.89–2.34) | <0.001 |

[†]The non-parametric Kruskal-Wallis test, P<0.05 indicates a statistically significant difference. SNR, signal-to-noise ratio; CNR, contrast-to-noise ratio.

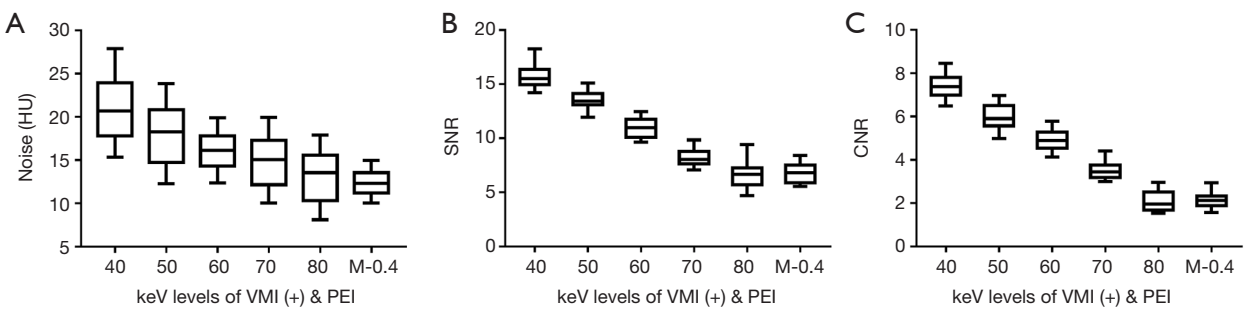


**Figure 3** Objective image characteristics for VMIs (+) at 40–80 keV and PEI (M_0.4). The 40 keV VMI (+) reconstructed by contrast-enhanced phase images gained the highest noise, SNR, and CNR values compared with 50–80 keV VMIs (+) and PEI (M_0.4). VMI (+), noise-optimized virtual monoenergetic images; keV, kiloelectron volt; PEI (M_0.4), polyenergetic images with a mix factor of 0.4; SNR, signal-to-noise ratio; CNR, contrast-to-noise ratio.

 

**Table 3** Image features of 40 keV VMI (+) in the enhanced phase

| Parameters | $NPC_{T1}$ (n=44) | BH (n=47) | P value |
|---|---|---|---|
| Tumor symmetry | 16/44 (36.4%) | 35/47 (74.5%) | <0.001 |
| Density homogeneity | 30/44 (68.2%) | 36/47 (76.6%) | 0.369 |
| Degree of enhancement | | | |
| High | 3/44 (6.8 %) | 3/47 (8.5%) | 0.762 |
| Intermediate | 28/44 (63.6%) | 28/47 (59.6%) | 0.691 |
| Low | 13/44 (29.5%) | 16/47 (36.2%) | 0.502 |

Data are presented as the number (percentage). VMI (+), noise-optimized virtual monoenergetic images; $NPC_{T1}$, stage T1 nasopharyngeal carcinoma; BH, benign hyperplasia.

**Table 4** Multiple quantitative parameters derived from DECT between stage T1 nasopharyngeal carcinoma ($NPC_{T1}$) and benign hyperplasia (BH)

| Parameters | $NPC_{T1}$ | BH | t value | P value |
|---|---|---|---|---|
| NIC | 0.34±0.07 | 0.26±0.06 | 6.037 | <0.001 |
| $\lambda_{HU}$ (HU/keV) | 2.30±0.53 | 1.83±0.45 | 4.568 | <0.001 |
| $NZ_{eff}$ | 0.84±0.04 | 0.80±0.04 | 4.175 | <0.001 |
| $A_{40}$ (HU) | 163.56±23.75 | 143.37±22.62 | 4.154 | <0.001 |
| $A_{50}$ (HU) | 125.28± 19.02 | 117.27±20.40 | 1.931 | 0.057 |
| $A_{60}$ (HU) | 98.71±15.44 | 93.34±16.55 | 1.599 | 0.113 |
| $A_{70}$ (HU) | 79.03±11.09 | 74.83±10.53 | 1.850 | 0.068 |
| $A_{80}$ (HU) | 69.20±10.29 | 67.01±8.99 | 1.086 | 0.281 |
| $A_n$ | 36.13±8.45 | 33.30±8.62 | 1.581 | 0.117 |
| $A_e$ | 69.40±11.40 | 71.00±11.82 | –0.657 | 0.513 |
| ΔA | 33.27±12.93 | 37.70±13.60 | –1.591 | 0.115 |

Data are presented as the mean ± standard deviation. Independent sample t-test was used. P value <0.050 indicates statistically significant difference. VMI (+), noise-optimized virtual monoenergetic images; $A_{40–80}$, attenuation value in 40–80 keV VMIs (+); NIC, normalized iodine concentration; $\lambda_{HU}$, slope of the spectral Hounsfield unit curve; $NZ_{eff}$, normalized effective atomic number; $A_n$, attenuation value in nonenhanced polyenergetic images; $A_e$, attenuation value in contrast-enhanced polyenergetic images; ΔA, $A_e$ $A_n$.

## Discussion

Our findings showed that 40 keV VMI (+) provided the optimal visualization of $NPC_{T1}$ and BH, and combined image features with quantitative parameters yielded the best performance for differentiating the 2 entities, with an AUC of 0.963, a sensitivity of 89.4%, and a specificity of 93.2%.

DECT could yield VMIs at low-energy levels, increasing image contrast and reducing artifacts, enabling improvement of tumor discrimination (25-27). In our study, 40 keV VMI (+) in the contrast-enhanced phase yielded the highest subjective image quality scores, SNR and CNR, to detect $NPC_{T1}$. Similar findings were also reported by previous studies (11,12), which found that 40 keV VMI (+) obtained the highest image quality for tumor delineation in head and neck imaging. However, there were inconsistent findings in previous studies for the head and neck. One study reported that the subjective overall image quality, CNR, and tumor delineation of 60 keV VMI was optimal (28), while another study showed that the optimal image SNR was at 65 keV VMI (11). The reason for these differences could be that the latest VMI (+) reconstruction technology utilized in our study, which used a regional spatial frequency-based recombination of higher signals at lower energies and avoided the increased noise at lower calculated energies, might further improve the SNR

 

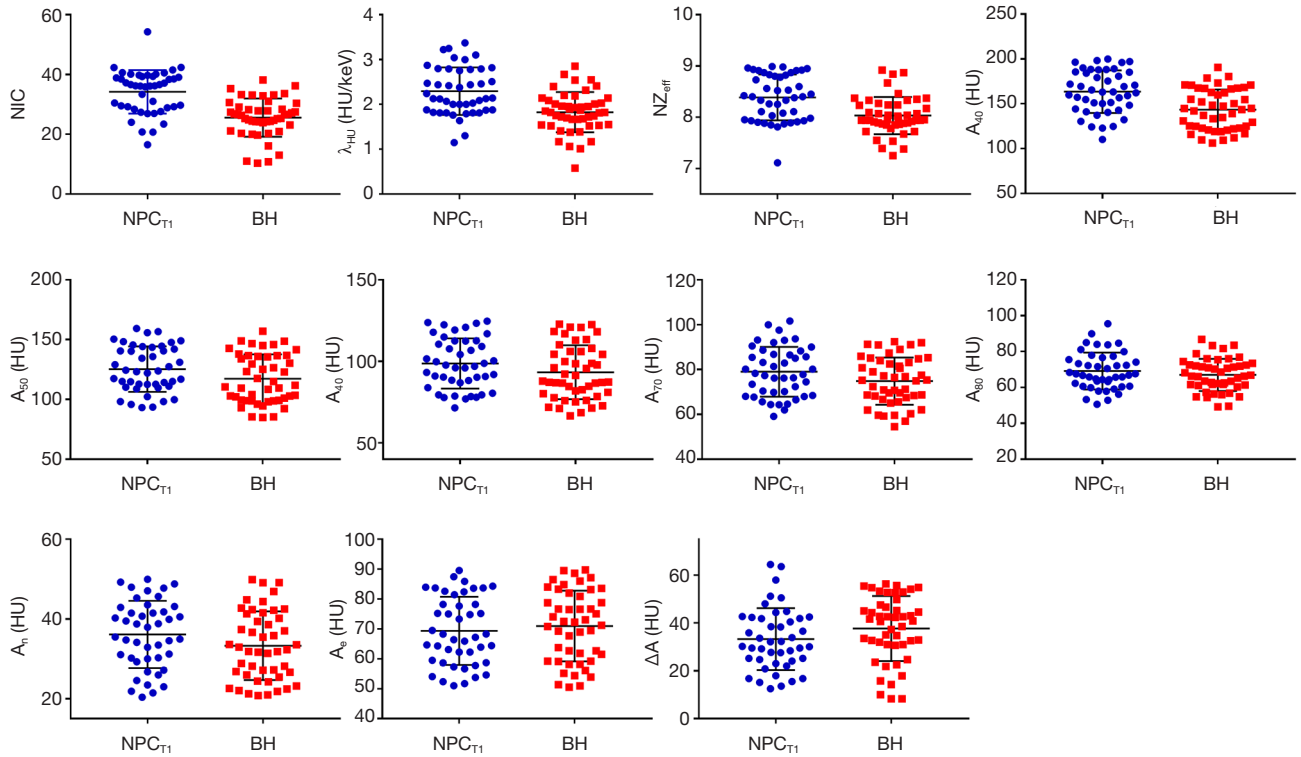


**Figure 4** Quantitative parameters derived from DECT of NPCT1 and BH. The $A_{40}$, NIC, $\lambda_{HU}$, and $NZ_{eff}$ values of $NPC_{T1}$ were significantly higher than BH. However, the $A_{50}$, $A_{60}$, $A_{70}$, $A_{80}$, $A_n$, $A_e$, and ΔA showed no differences between the 2 entities. DECT, dual-energetic computed tomography; $NPC_{T1}$, stage T1 nasopharyngeal carcinoma; BH, benign hyperplasia; NIC, normalized iodine concentration; $\lambda_{HU}$, slope of the spectral Hounsfield unit curve; $NZ_{eff}$, normalized effective atomic number; VMI (+), noise-optimized virtual monoenergetic images; $A_{40-80}$, attenuation value in 40–80 keV VMIs (+); $A_n$, attenuation value in nonenhanced polyenergetic images; $A_e$, attenuation value in enhanced polyenergetic images; ΔA, $A_e$–$A_n$.

and CNR at 40 keV (29).

IC allowed the lesion's vascular enhancement to be quantifiably measured, which helped identify benign and malignant tumors (30). The NIC minimized the variations caused by the patients' different circulation statuses and scanning times. Our study showed that the NIC in the enhanced phase successfully distinguished $NPC_{T1}$ from BH, consistent with a previous DECT study in NPC (31). $NPC_{T1}$ was characterized by abundant tumor angiogenesis and incomplete vascular endothelium, resulting in higher iodine contrast accumulation than BH (32). In our study, the NIC yielded a slightly lower AUC value (0.825) than the AUC value (0.880) of NIC in the abovementioned study. This difference in results might have been due to differences in the sample sizes and image reconstructions of the 2 studies (33).

The quantitative $Z_{eff}$ represented the composite atom for a mixture or compound of various materials and helped distinguish benign and malignant tumors (18). Our data showed that $NPC_{T1}$ had higher $Z_{eff}$ values than BH, which was consistent with a previous study (31). The possible reason was that $NPC_{T1}$ was characterized by closely packed tumor cells with a higher nuclear-cytoplasmic ratio in histopathology, leading to a higher $Z_{eff}$ than BH (34).

The energy spectrum curves represented the change characteristics of CT values with the change of X-ray energy. In theory, each material had its specific $\lambda_{HU}$ enabling the differentiation of benign and malignant tumors (35). Our results found that $NPC_{T1}$ yielded higher $\lambda_{HU}$ values than BH. This result was consistent with previous studies. Compared with BH, the more contrast agent leakage in NPCs could result in stronger spectral properties, providing a steeper attenuation curve and higher $\lambda_{HU}$ value (31).

In our study, combined image features with quantitative

 

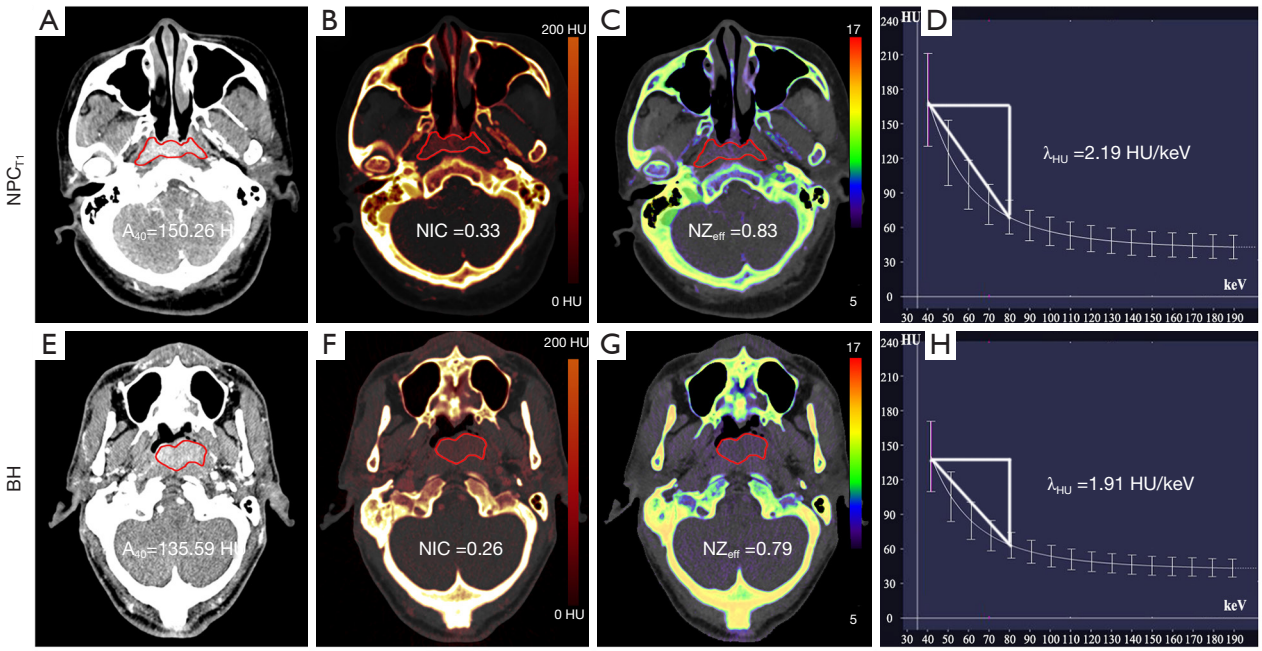


**Figure 5** The noise-optimized virtual monoenergetic images 40 keV VMIs (+) (A,E), iodine-water maps (B,F), effective atomic number maps (C,G), and spectral Hounsfield unit curves (D,H) for a 65-year-old man with $NPC_{T1}$ and a 50-year-old woman with BH, respectively. NPCT1 gained the higher $A_{40}$, NIC, $\lambda_{HU}$, and $NZ_{eff}$ values compared with BH (all P values <0.001). VMI (+), noise-optimized virtual monoenergetic images; $NPC_{T1}$, stage T1 nasopharyngeal carcinoma; BH, benign hyperplasia; $A_{40}$, attenuation value in 40 keV VMI (+); NIC, normalized iodine concentration; $NZ_{eff}$, normalized effective atomic number; $\lambda_{HU}$, slope of the spectral Hounsfield unit curve.

**Table 5** Diagnostic performance of image feature and quantitative parameters in differentiating stage T1 nasopharyngeal carcinoma and benign hyperplasia

| Parameters | Cutoff value | AUC | Sensitivity (%) | Specificity (%) |
|---|---|---|---|---|
| Tumor symmetry | 0.500 | 0.691 | 63.6 | 74.5 |
| $A_{40}$ (HU) | 150.301 | 0.727 | 72.7 | 61.7 |
| NIC | 28.385 | 0.825 | 79.5 | 74.5 |
| $\lambda_{HU}$ | 1.900 | 0.744 | 70.5 | 68.1 |
| $NZ_{eff}$ | −0.810 | 0.732 | 68.2 | 68.1 |
| Combined | 0.567 | 0.963* | 89.4 | 93.2 |

*, in the multivariate logistic regression model, the combination of image feature and quantitative parameters yielded the highest AUC, with all P values <0.05. VMI (+), noise-optimized virtual monoenergetic images; $A_{40}$, attenuation value in 40 keV VMIs (+); NIC, normalized iodine concentration; $\lambda_{HU}$, slope of the spectral Hounsfield unit curve; $NZ_{eff}$, normalized effective atomic number; combined, combined image feature (tumor symmetry) with quantitative parameters ($A_{40}$, NIC, $\lambda_{HU}$, and $Z_{eff}$).

parameters yielded the best performance for differentiating $NPC_{T1}$ from BH, with an AUC of 0.963, a sensitivity of 89.4%, and a specificity of 93.2%. The possible reason is that the image features only reflect macroscopic information of lesion morphology, while the quantitative parameters can reflect microscopic information such as blood flow and material composition. The combination of the 2 can more accurately reveal the essential characteristics of the lesions.

There were some limitations in our study. First, because of our study's small sample size, large sample and multi-

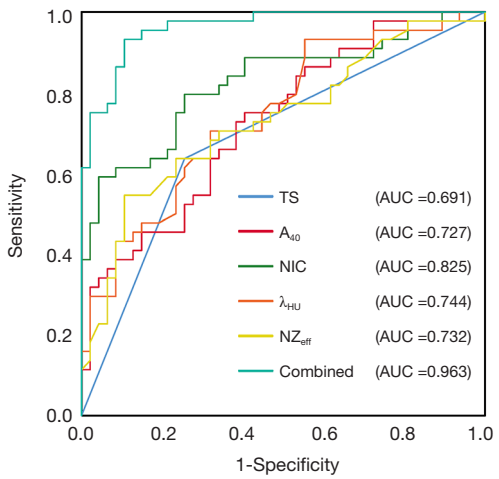


**Figure 6** ROC analyses of image features and quantitative parameters for differentiating $NPC_{T1}$ from BH. The multivariate logistic regression model combining image features (tumor symmetry) with quantitative parameters ($A_{40}$, NIC, $\lambda_{HU}$, and $NZ_{eff}$) yielded higher AUC (0.963), sensitivity (89.4%), and specificity (93.2%) values than any 1 parameter alone. In terms of AUC, all P values were less than 0.05. ROC, receiver operating characteristic; $NPC_{T1}$, stage T1 nasopharyngeal carcinoma; BH, benign hyperplasia; TS, tumor symmetry; $A_{40}$, attenuation value in 40 keV VMIs (+); NIC, normalized iodine concentration; $\lambda_{HU}$, slope of the spectral Hounsfield unit curve; $NZ_{eff}$, normalized effective atomic number; combined, image feature combined with quantitative parameters using multivariate logistic regression.

center studies are needed to further improve the results' reliability. Second, MRI and DECT's performance in the differential diagnosis of BH and $NPC_{T1}$ was not compared. This comparison should be performed in future research to provide better imaging methods for differentiating the 2 entities.

In conclusion, the combination of DECT-derived image features and quantitative parameters contributed to the differentiation between $NPC_{T1}$ and BH. Therefore, our study results will be beneficial for the treatment and prognosis improvement in patients with NPC.

## Acknowledgments

*Funding:* This study has received funding from the National Natural Science Foundation of China (Grant No. 82071883), the combination projects of medicine and engineering of the Fundamental Research Funds for the Central Universities in 2019 (Project No. 2019CDYGYB008), the Chongqing key medical research project of a combination of science and medicine (Grant No. 2019ZDXM007), the 2019 SKY Imaging Research Fund of the Chinese International Medical Foundation (Project No. Z-2014-07-1912-10), Chongqing medical research project of a combination of science and medicine (Grant No. 2021MSXM077), and Chongqing medical research project of a combination of science and medicine (Grant No. 2021MSXM035).

## Footnote

*Conflicts of Interest:* All authors have completed the ICMJE uniform disclosure form (available at http://dx.doi.org/10.21037/qims-20-1269). The authors have no conflicts of interest to declare.

*Ethical Statement:* The authors are accountable for all aspects of the work in ensuring that questions related to the accuracy or integrity of any part of the work are appropriately investigated and resolved. The study was conducted in accordance with the Declaration of Helsinki (as revised in 2013). The study was approved by the ethics committee of the Chongqing University Cancer Hospital, and written informed consent was obtained.



## References

1. Bhatia KS, King AD, Vlantis AC, Ahuja AT, Tse GM. Nasopharyngeal mucosa and adenoids: appearance at MR imaging. Radiology 2012;263:437-43.
2. Chen YP, Chan ATC, Le QT, Blanchard P, Sun Y, Ma J. Nasopharyngeal carcinoma. Lancet 2019;394:64-80.
3. King AD, Vlantis AC, Bhatia KS, Zee BC, Woo JK, Tse GM, Chan AT, Ahuja AT. Primary nasopharyngeal carcinoma: diagnostic accuracy of MR imaging versus that of endoscopy and endoscopic biopsy. Radiology

 

2011;258:531-7.
4. King AD, Vlantis AC, Yuen TW, Law BK, Bhatia KS, Zee BC, Woo JK, Chan AT, Chan KC, Ahuja AT. Detection of Nasopharyngeal Carcinoma by MR Imaging: Diagnostic Accuracy of MRI Compared with Endoscopy and Endoscopic Biopsy Based on Long-Term Follow-Up. AJNR Am J Neuroradiol 2015;36:2380-5.
5. King AD, Wong LYS, Law BKH, Bhatia KS, Woo JKS, Ai QY, Tan TY, Goh J, Chuah KL, Mo FKF, Chan KCA, Chan ATC, Vlantis AC. MR Imaging Criteria for the Detection of Nasopharyngeal Carcinoma: Discrimination of Early-Stage Primary Tumors from Benign Hyperplasia. AJNR Am J Neuroradiol 2018;39:515-23.
6. King AD, Woo JKS, Ai QY, Mo FKF, So TY, Lam WKJ, Tse IOL, Vlantis AC, Yip KWN, Hui EP, Ma BBY, Chiu RWK, Chan ATC, Lo YMD, Chan KCA. Early Detection of Cancer: Evaluation of MR Imaging Grading Systems in Patients with Suspected Nasopharyngeal Carcinoma. AJNR Am J Neuroradiol 2020;41:515-21.
7. Ai QY, King AD, Chan JSM, Chen W, Chan KCA, Woo JKS, Zee BCY, Chan ATC, Poon DMC, Ma BBY, Hui EP, Ahuja AT, Vlantis AC, Yuan J. Distinguishing early-stage nasopharyngeal carcinoma from benign hyperplasia using intravoxel incoherent motion diffusion-weighted MRI. Eur Radiol 2019;29:5627-34.
8. Wang ML, Wei XE, Yu MM, Li WB. Value of contrast-enhanced MRI in the differentiation between nasopharyngeal lymphoid hyperplasia and T1 stage nasopharyngeal carcinoma. Radiol Med 2017;122:743-51.
9. McCollough CH, Leng S, Yu L, Fletcher JG. Dual- and Multi-Energy CT: Principles, Technical Approaches, and Clinical Applications. Radiology 2015;276:637-53.
10. Goo HW, Goo JM. Dual-Energy CT: New Horizon in Medical Imaging. Korean J Radiol 2017;18:555-69.
11. Lam S, Gupta R, Levental M, Yu E, Curtin HD, Forghani R. Optimal Virtual Monochromatic Images for Evaluation of Normal Tissues and Head and Neck Cancer Using Dual-Energy CT. AJNR Am J Neuroradiol 2015;36:1518-24.
12. May MS, Bruegel J, Brand M, Wiesmueller M, Krauss B, Allmendinger T, Uder M, Wuest W. Computed Tomography of the Head and Neck Region for Tumor Staging-Comparison of Dual-Source, Dual-Energy and Low-Kilovolt, Single-Energy Acquisitions. Invest Radiol 2017;52:522-8.
13. Albrecht MH, Vogl TJ, Martin SS, Nance JW, Duguay TM, Wichmann JL, De Cecco CN, Varga-Szemes A, van Assen M, Tesche C, Schoepf UJ. Review of Clinical Applications for Virtual Monoenergetic Dual-Energy CT. Radiology 2019;293:260-71.
14. Martin SS, Albrecht MH, Wichmann JL, Hüsers K, Scholtz JE, Booz C, Bodelle B, Bauer RW, Metzger SC, Vogl TJ, Lehnert T. Value of a noise-optimized virtual monoenergetic reconstruction technique in dual-energy CT for planning of transcatheter aortic valve replacement. Eur Radiol 2017;27:705-14.
15. De Cecco CN, Caruso D, Schoepf UJ, De Santis D, Muscogiuri G, Albrecht MH, Meinel FG, Wichmann JL, Burchett PF, Varga-Szemes A, Sheafor DH, Hardie AD. A noise-optimized virtual monoenergetic reconstruction algorithm improves the diagnostic accuracy of late hepatic arterial phase dual-energy CT for the detection of hypervascular liver lesions. Eur Radiol 2018;28:3393-404.
16. Lv P, Lin XZ, Li J, Li W, Chen K. Differentiation of small hepatic hemangioma from small hepatocellular carcinoma: recently introduced spectral CT method. Radiology 2011;259:720-9.
17. Yuan Y, Zhang Y, Lang N, Li J, Yuan H. Differentiating malignant vertebral tumours from non-malignancies with CT spectral imaging: a preliminary study. Eur Radiol 2015;25:2945-50.
18. González-Pérez V, Arana E, Barrios M, Bartrés A, Cruz J, Montero R, González M, Deltoro C, Martínez-Pérez E, De Aguiar-Quevedo K, Arrarás M. Differentiation of benign and malignant lung lesions: Dual-Energy Computed Tomography findings. Eur J Radiol 2016;85:1765-72.
19. Al-Najami I, Mahmoud Sheta H, Baatrup G. Differentiation between malignant and benign rectal tumors by dual-energy computed tomography - a feasibility study. Acta Oncol 2019;58:S55-9.
20. Forghani R. An update on advanced dual-energy CT for head and neck cancer imaging. Expert Rev Anticancer Ther 2019;19:633-44.
21. Pérez-Lara A, Forghani R. Spectral Computed Tomography: Technique and Applications for Head and Neck Cancer. Magn Reson Imaging Clin N Am 2018;26:1-17.
22. Forghani R, Kelly HR, Curtin HD. Applications of Dual-Energy Computed Tomography for the Evaluation of Head and Neck Squamous Cell Carcinoma. Neuroimaging Clin N Am 2017;27:445-59.
23. Guo R, Tang LL, Mao YP, Du XJ, Chen L, Zhang ZC, Liu LZ, Tian L, Luo XT, Xie YB, Ren J, Sun Y, Ma J. Proposed modifications and incorporation of plasma Epstein-Barr virus DNA improve the TNM staging system

 

for Epstein-Barr virus-related nasopharyngeal carcinoma. Cancer 2019;125:79-89.
24. Shen H, Yuan X, Liu D, Huang Y, Wang Y, Jiang S, Zhang J. Multiparametric dual-energy CT for distinguishing nasopharyngeal carcinoma from nasopharyngeal lymphoma. Eur J Radiol 2021;136:109532.
25. Beer L, Toepker M, Ba-Ssalamah A, Schestak C, Dutschke A, Schindl M, Wressnegger A, Ringl H, Apfaltrer P. Objective and subjective comparison of virtual monoenergetic vs. polychromatic images in patients with pancreatic ductal adenocarcinoma. Eur Radiol 2019;29:3617-25.
26. Darras KE, Clark SJ, Kang H, Mohammed MF, Barrett S, Chang SD, Harris AC, Nicolaou S, McLaughlin PD. Virtual monoenergetic reconstruction of contrast-enhanced CT scans of the abdomen and pelvis at 40 keV improves the detection of peritoneal metastatic deposits. Abdom Radiol (NY) 2019;44:422-8.
27. Schabel C, Patel B, Harring S, Duvnjak P, Ramirez-Giraldo JC, Nikolaou K, Nelson RC, Farjat AE, Marin D. Renal Lesion Characterization with Spectral CT: Determining the Optimal Energy for Virtual Monoenergetic Reconstruction. Radiology 2018;287:874-83.
28. Wichmann JL, Noske EM, Kraft J, Burck I, Wagenblast J, Eckardt A, Frellesen C, Kerl JM, Bauer RW, Bodelle B, Lehnert T, Vogl TJ, Schulz B. Virtual monoenergetic dual-energy computed tomography: optimization of kiloelectron volt settings in head and neck cancer. Invest Radiol 2014;49:735-41.
29. Lenga L, Czwikla R, Wichmann JL, Leithner D, Albrecht MH, Booz C, Arendt CT, Yel I, D'Angelo T, Vogl TJ, Martin SS. Dual-energy CT in patients with colorectal cancer: Improved assessment of hypoattenuating liver metastases using noise-optimized virtual monoenergetic imaging. Eur J Radiol 2018;106:184-91.
30. Kato T, Uehara K, Ishigaki S, Nihashi T, Arimoto A, Nakamura H, Kamiya T, Oshiro T, Ebata T, Nagino M. Clinical significance of dual-energy CT-derived iodine quantification in the diagnosis of metastatic LN in colorectal cancer. Eur J Surg Oncol 2015;41:1464-70.
31. Wang P, Xiao Z, Tang Z, Wang J. Dual-energy CT in the differentiation of stage T1 nasopharyngeal carcinoma and lymphoid hyperplasia. Eur J Radiol 2020;124:108824.
32. Song C, Cheng P, Cheng J, Zhang Y, Sun M, Xie S, Zhang X. Differential diagnosis of nasopharyngeal carcinoma and nasopharyngeal lymphoma based on DCE-MRI and RESOLVE-DWI. Eur Radiol 2020;30:110-8.
33. Euler A, Solomon J, Mazurowski MA, Samei E, Nelson RC. How accurate and precise are CT based measurements of iodine concentration? A comparison of the minimum detectable concentration difference among single source and dual source dual energy CT in a phantom study. Eur Radiol 2019;29:2069-78.
34. Petersson F. Nasopharyngeal carcinoma: a review. Semin Diagn Pathol 2015;32:54-73.
35. Liu X, Ouyang D, Li H, Zhang R, Lv Y, Yang A, Xie C. Papillary thyroid cancer: dual-energy spectral CT quantitative parameters for preoperative diagnosis of metastasis to the cervical lymph nodes. Radiology 2015;275:167-76.

**Cite this article as:** Shen H, Yuan X, Liu D, Tu C, Wang X, Liu R, Wang X, Lan X, Fu K, Zhang J. Multiparametric dual-energy CT to differentiate stage T1 nasopharyngeal carcinoma from benign hyperplasia. Quant Imaging Med Surg 2021;11(9):4004-4015. doi: 10.21037/qims-20-1269

 